Time-resolved spatial patterns and interactions of soot, PAH and OH in a turbulent diffusion flame

B. Franzelli, P. Scouflaire, S. Candel

Time-resolved spatial patterns and interactions of soot, PAH and OH in a turbulent diffusion flame

B. Franzelli[a,b,*], P. Scouflaire[a,b], S. Candel[a,b]

[a] *Ecole Centrale Paris, Grande Voie des Vignes, 92290 Châtenay-Malabry, France*
[b] *CNRS, UPR 288, Laboratoire d'Energétique Moléculaire et Macroscopique, Combustion (EM2C), Grande Voie des Vignes, 92290 Châtenay-Malabry, France*

Abstract

Soot control raises important fundamental issues and industrial challenges, which require a comprehensive understanding of processes governing its formation, interactions and destruction in turbulent flames. A physical insight of the soot space-time evolution in a turbulent diffusion flame is reported in this article by combining three simultaneous high sampling rate imaging diagnostics operating at a frame rate of 10 kHz: light scattering from soot particles, planar laser induced fluorescence (PLIF) of the OH radical, a marker of the flame region, and planar laser induced fluorescence of Polycyclic Aromatic Hydrocarbons (PAHs), classically identified as soot precursors. Images issued from these diagnostics provide a spatially resolved information on the production of soot, its interaction with the turbulent flow and its link with the flame surface and with soot precursors regions. It is shown in particular that soot pockets are highly distorted by turbulent eddies forming a characteristic layered pattern. A statistical analysis is also proposed to analyze such high-speed imaging results. Information on soot-OH-PAH correlation deduced from the high speed imaging could be employed to verify the adequacy of models devised to represent soot dynamics in direct or large eddy simulations of turbulent flames.

Keywords: Soot-OH-PAH interaction, turbulent flames, high frame-rate simultaneous measurements, PLIF OH and PLIF PAH, soot light scattering.

*Corresponding author
Email address: benedetta.franzelli@ecp.fr (B. Franzelli)

1. Introduction

Soot particles, generated by combustion in many practical devices such as Diesel engines or gas turbines, have a negative impact on the environment and on public health. Reducing these emissions constitutes a fundamental and industrial challenge requiring a detailed understanding of soot generation and oxidation in flames and, more specifically, in turbulent flames that correspond to most practical applications.

Soot production is a complex process implying nucleation from soot precursors, surface growth by chemical and collisional processes, interaction with the reactive flow and partial destruction by oxidation in the flame. Many experimental and numerical efforts have been made in the last fifty years to characterize and model these processes, see for example [1, 2, 3, 4]. Nevertheless, these phenomena are not fully understood even for laminar flows and soot modelling validation is still often limited by difficulties in extracting experimental information, such as the particle number density, size distribution and volume fraction [4].

In comparison with the laminar flame case, soot production in turbulent flames is even more complex because it depends also on the flow history and on local turbulence properties [5, 6, 7]. Experiments on turbulent flames are essential to address practical issues. In this respect, progress has been accomplished with the development of Laser Induced Incandescence (LII), which allows soot concentration quantification [8]. Recent experiments of Lee et al. [9] and Köhler et al. [7] provide original information on turbulent sooting flames based on LII of soot concentration together with distributions of PAHs, considered as the principal soot precursors, and OH radicals. Such low frame-rate and non-simultaneous measurements provide a mean description of the flame structure but are not sufficient to observe the local space-time history. In contrast, simultaneous measurements of local quantities like OH and PAH and soot constitute a promising way to investigate the dependence of soot concentration on local flow conditions. Simultaneous measurements of soot and OH [10] or soot and flow velocity [11] provide interesting relations between soot concentration, flame front location and particle residence time, respectively. Such low frame rate measurements do not convey crucial information on soot evolution, which is characterized by strong intermittency and dynamical features [12].

The present work aims at advancing the understanding of the processes that underlie soot formation, interactions and destruction in turbulent flames through simultaneous space-time measurements. Analysis relies on high sampling rate imaging operating at 10 kHz and allowing observations of an essentially multi-scale unsteady phenomenon. Three films are recorded synchronously combining light scattering (LS) from soot particles, planar laser induced fluorescence (PLIF) of the OH radical (a marker of the flame region) and planar laser induced fluorescence of PAHs, the soot precursors. These diagnostics provide space-time information on the production of soot and its link with the flame front and with PAH precursors in turbulent flows.

Admittedly, light scattering only provides a qualitative characterization of soot distribution, but it is here used instead of LII to obtain a high temporal resolution which is not accessible with LII due to laser power constraints. To our knowledge, this is the first time that the temporal and spatial evolution of the layered structure and the high intermittency of soot is experimentally observed revealing links between soot, OH and precursors in a typical non-premixed turbulent flame. A statistical analysis is also proposed to analyze imaging data which could be used to guide modeling efforts for the prediction of soot with large eddy or direct simulations.

The experimental configuration, optical setup and processing methods are described in Section 2. Results are presented in Section 3 and the soot formation and growth regions are characterized using statistical tools in Section 4.

2. Experimental setup and data processing

Experiments are carried out on a turbulent diffusion flame established by a coaxial injector. The inner jet of gaseous methane is surrounded by an annular flow of pure oxygen allowing stabilization at injector lips even for very high Reynolds numbers.[1] The inner methane injector has a diameter of $d = 0.39$ cm and wall thickness of 0.12 cm. The external O_2 injection tube has a diameter of 1 cm. Methane and oxygen mass flow rates correspond to Reynolds numbers $\mathrm{Re}_{CH_4} = 7000$ and $\mathrm{Re}_{O_2} = 700$, respectively.

The injector can be displaced in the vertical direction allowing measurements over the whole flame region. The optical setup is represented in Fig. 1. A Nd:YAG laser (Edgewave) generating pulses at 532 nm with an energy of 10 mJ, a duration of 1ns and a repetition rate $f = 10$ kHz pumps a dye laser (Radiant) circulating Rhodamine 590 dissolved in methanol. This is followed by a frequency doubler with an output centered on the Q1(6) OH transition in the A-X(1-0) band at a wavelength $\lambda = 282.92$nm and a pulse energy of 200 μJ. A laser sheet generator (Melles Griot system) is used to create a planar beam of thickness equal to $0.1d \approx 0.4$ mm. It passes through the injector axis and extends vertically over $8d \approx 3$ cm.

Three high speed Photron intensified CMOS cameras (SAX, SA5, APX) are placed at 90° with respect the laser sheet. SAX and SA5 cameras are equipped with external Hamamatsu intensifiers (C10880-03C with a A4539 lens) while the APX head comprises an intensifier. The SAX camera captures OH fluorescence with an exposure time of $\tau^{OH} = 30$ ns. It is equipped with a filter centered at 310 nm with a full width at half maximum (FWHM) of 10 nm. This filter is well adapted to the detection of OH fluorescence. It is also sufficiently narrow to reduce the interference with PAH fluorescence which occurs over a broader band of wavelengths. Indeed, the final contribution of PAH fluorescence to the signal in the filter band is expected to be negligible compared to that originating from OH as can be deduced for

[1] The impact of the oxygen injection is assumed to have small effect on the flame structure compared to no annular injection case.

example from [13] (although for a different pumping scheme) and as can be verified by operating in an off-resonance mode. When the laser does not match an OH absorption line, there is essentially no signal.

The second SA5 camera records PAH fluorescence using a band-pass filter centered at 377 nm (FWHM of 50 nm), which cuts-off OH fluorescence, and an exposure time of $\tau^{PAH} = 200$ ns [14] . It has been verified that the OH* emission is essentially reduced by the filter. LII interference with the PAH signal is unlikely because the laser fluence of ≈ 1.3 mJ/cm^2 is smaller than the one required to activate incandescence (≈ 2 mJ/cm^2) and smaller than that typically used in LII imaging experiments [9, 15, 16].

The APX camera exposure time is set at $\tau^{LS} = 200$ ns to record soot light scattering. A shorter exposure could have been selected for laser scattering imaging but a higher value was adopted to guarantee capturing the scattered light at each laser pulse taking care of possible jitter in the triggering system. This is much smaller than $10\mu s$ which was found sufficient to suppress light emission interference. Fluorescence from OH and PAH are shifted with respect to the scattered light and could have been filtered out. This was not needed because the intensifier gain of the APX camera used to collect scattered light was well below values required to record OH or PAH fluorescence (i.e. the dynamic range of the camera essentially fits scattered light signals).

All cameras are synchronized with the laser pulse with a delay between the pulse and the camera gate opening for both OH and PAH measurements. The experimental setup has been verified by comparing instantaneous images corresponding to light scattering with three cameras.

There are differences in the spatial resolutions of the three cameras: $\Delta x^{LS} \approx 0.06d$, $\Delta x^{OH} \approx 0.03d$ and $\Delta x^{PAH} \approx 0.035d$. These values are sufficient to resolve soot layers which have a typical thickness $\theta^{soot} = 0.1 - 0.6d$ [9]. In the data processing, the mean beam intensity along the vertical laser sheet is used to correct signals for variations in intensity. Measurements from the three cameras are spatially interpolated in a two-dimensional matrix to get information for all quantities at each point. Signals are then stored into three 3-D matrices: $\mathbf{I}(x, y, t) \in \mathbb{R}_+^{N_x \times N_y \times N_t}$, with $N_x = 40d/\Delta x^{OH}$, $N_y = 3d/\Delta x^{OH}$ and $N_t = 0.1s * 10$ kHz. A representative snapshot obtained by combining signals from the three cameras is shown in Fig. 2a. Red to yellow scale represents OH-PLIF, a blue colormap is used for PAH-PLIF while soot LS intensity is reproduced in orange. To obtain a presence index the signal intensities are converted into binary form:

$$P(I_{ijk}) = \begin{cases} 1 & \text{if } I_{ijk} > \epsilon \\ 0 & \text{if } I_{ijk} = \epsilon \end{cases} \tag{1}$$

Camera noise is reduced by setting a threshold ϵ based on the maximum signal value. Below the threshold, the presence index is equal to zero. The binary signals, represented in Fig. 2b. for the measurements discussed in Fig. 2a, are used in what follows to identify the spatial locations of the quantities of interest.

3. Flame structure

The soot structure of the coaxial turbulent flame, represented in Fig. 3a, is characterized by considering the formation, growth and mixing regions. Simultaneous measurements of PLIF PAH, PLIF OH and soot light scattering have been recorded for the whole flame length. Figures 3b-g show results for six positions ($h = 2, 7, 18, 39, 80, 135d$) which typify the different flame regions. For each location the three measurements are recorded simultaneously, but images at different measurement positions correspond to different instants. PAH, OH and soot signal intensities vary along the flame. However, for the sake of clarity, all signals in Fig. 3 have been normalized by adjusting the color scales to the maximum intensity in each measurement region.

The flame is anchored on the injector lip, where two fronts are identified by the presence of OH (Fig. 3b). The OH signal is more intense in the injector nearfield where combustion is augmented by the presence of pure O_2. A laminar-like diffusion flame structure [2] is recognized at the second measurement position, where PAHs are first detected at about $10d$ (Fig. 3c). Here, methane is expected to be found in the core of the flame. The first aromatic species are formed in a rich mixture subsequently generating PAH in the form of ligaments. The sensitivity of the PAH level to strain rates induced by turbulence [17] is probably responsible for the heterogeneous appearance of the PAH sheet compared to the relatively smooth OH layer. Downstream ($h \approx 20d$), turbulence is fully developed and interacts with the species distributions (Fig. 3d). Soot precursors cease to form thin layers and occupy the core of the flame as observed in [7, 9].

Soot is first detected at $h \approx 30d$ and observed further downstream. In agreement with Lee et al. [9] one distinguishes three characteristic regions: a first region of soot formation (Fig. 3e, $h = 30 - 55d$), a second region where turbulent mixing takes place and the distribution of soot is mainly governed by vortical structures wrapping and stretching layers containing soot particles (Fig. 3f, $h = 55 - 100d$), a third region in which soot interacts with the flame, is oxidized and conveyed away from the flame (Fig. 3g, $h > 100d$).

These processes are now analyzed by examining the high frame-rate images. In Fig. 4 the presence indices P_{ijk} on the central line of the laser sheet ($j = N_y/2$) are plotted as a function of radial position ($i = 1, \ldots, N_x$) and time ($k = 1, \ldots, N_t$) in the three characteristic regions. In the formation and initial transport region (Fig. 4a), PAHs mainly arise in the central core of the flame and their distribution is more sensitive to the presence of turbulence than the OH signal. Soot is highly intermittent and its radial location is distinct from that of OH. Small soot pockets are mainly formed in the central part of the flame, whereas soot layers accumulate near the flame front marked by the OH fluorescence signal. This can be explained by examining Fig. 5a. Here, a small spot of soot is initially formed in the middle of the flame and moves radially from the PAH region to the flame front forming soot ligaments, which result from its interaction with turbulence. Soot layer coalescence as well as soot oxidation by OH and destruction due to

mixing and turbulence effects are also observed in this region (figure not shown). The temporal evolution of a soot layered structure, wrinkled and stretched by turbulence, is shown in Fig. 5b.

In the mixing-dominated region, soot is characterized by layers entrained by the large-scale eddies in the flow (Fig. 4b). Here, soot occupies a great portion of the flame and features a wrinkled pattern rapidly distorted by the flow. The distribution of soot layers seems to be correlated with PAH and is spatially confined by the lateral wrinkled flame fronts. Occasionally, when the flame front is highly wrinkled, stretched soot layers are engulfed by the OH layers. This case is shown in Fig. 6a. Here, the temporal evolution of the flame front as well as that of soot clearly indicate that soot oxidation is strongly related to OH-soot interaction. Some of the soot ligaments are detected inside the OH layers marking the flame but these soot regions are completely oxidized and no particles are seen to cross the flame radially.

At the flame tip (Fig. 4c) one recognizes a soot-oxidation region. Looking separately at the maximum values of OH and soot signals, Lee et al. [9] deduced that soot particles and OH fields overlapped in the soot-oxidation region of turbulent diffusion flames, leading to soot oxidation. In contrast with their findings the present simultaneous measurements indicate that OH and soot do not often overlap even in this region so that soot oxidation takes place in a different way. Soot is still detected at the tip of the flame, i.e. it is not completely oxidized before reaching the end of the flame. As classically observed in turbulent diffusion flames, the OH fluorescence layers are flapping at the flame termination and pockets of OH are seen to detach from the main flame (connections are still possible out of the image plane). Part of the soot ligaments follow these pockets where they finally disappear. The intermittency of OH and soot at the flame top could perhaps explain the conclusions reached by Lee et al. [9] from non simultaneous low frame rate imaging experiments. The soot-OH pockets oxidation phenomenon, revealed in Fig. 6b, provides an explanation for the incomplete soot oxidation leading to particle emission. The quantity of soot emitted in the surrounding atmosphere may depend on the way these soot pockets are created and on the rate at which they are oxidized. However, this could be strongly dependent on the third spatial direction of the flow and more investigations are required before concluding on the role of soot-OH pockets on final soot emission. The link of soot oxidation with the presence of OH is however clearly established.

4. Soot formation and growth

The formation and mixing-dominated soot regions are characterized by distinct patterns. It is now interesting to examine these processes with some statistical tools. It is convenient to define spatial averages of any quantity Q by:

$$\langle Q \rangle_k = \frac{1}{N_x N_y} \sum_{i=1}^{N_x} \sum_{j=1}^{N_y} Q_{ijk}. \tag{2}$$

The temporal evolution of $\langle I \rangle$ for soot (black), OH (red) and PAHs (blue) signals is plotted in Figs. 7a and Fig. 7b for the formation and mixing-dominated regions, respectively. OH features similar average and fluctuation values in both regions. In contrast, both soot and PAHs signals differ in the two regions with higher values and strong fluctuations in the mixing-dominated region.

The occupation ratio $\langle P(I) \rangle$ is obtained by spatially averaging the presence index. This defines the image portion occupied by the quantity of interest and reflects the presence or absence of a particular quantity. The occupation ratios of soot, OH and PAHs are represented in Fig. 8 for both regions. Once again, a similar behavior is observed for OH in both formation and mixing-dominated regions, implying that the flame front occupies the same relative area in both regions. Regarding soot, the occupation ratio $\langle P(I^{soot}) \rangle$ drastically increases in the mixing-dominated region as already discussed in Section 3.1. The soot spatial average $\langle I^{soot} \rangle$ increases in the mixing-dominated region indicating that soot is broadly distributed in this region, so that the soot signal features the same level in both regions. In contrast, the occupation ratio $\left\langle P(I^{PAH}) \right\rangle$ is nearly the same in both regions, whereas its mean value $\left\langle I^{PAH} \right\rangle$ drastically increases in the mixing-dominated region. Indeed, PAH signal intensity presents a higher value in the mixing-dominated region. Finally, the occupation ratio $\left\langle P(I^{OH}) \right\rangle$ has small temporal fluctuations compared to PAHs and soot which both feature higher levels of fluctuation and a greater sensitivity to turbulence. It is also interesting to examine the spatial correlation r_p^{lm}:

$$r_p^{lm} = \frac{\sigma^{lm}}{\sqrt{\sigma^{ll}}\sqrt{\sigma^{mm}}} \tag{3}$$

This index could be used to identify a possible dependence in the spatial location of quantities l and m. σ^{ll} is the square of the standard deviation of $P(I^l)$ and σ^{lm} is the covariance between $P(I^l)$ and $P(I^m)$, such that:

$$\sigma^{lm} = \left\langle \left(P(I_k^l) - \left\langle P(I_{ijk}^l) \right\rangle \right) \cdot \left(P(I_{ijk}^m) - \left\langle P(I_{ijk}^m) \right\rangle \right) \right\rangle . \tag{4}$$

Near-unity values identify a linear correlation, near-zero values are obtained for independent variables, whereas an anti-correlation could be established for negative values. Temporal evolution of soot-PAH, soot-OH and OH-PAH correlations are plotted in Fig. 9 for both formation and mixing-dominated regions (blue, red, black lines, respectively). OH and PAH (black line) are characterized by a negative dependence since, as already discussed in Section 3.1, they occur in distinct regions for both formation and mixing-dominated soot regions. The OH-soot spatial correlation (red line) shows an independent behavior in the formation region, mainly because soot arises in small and intermittent spots in this region. In contrast, in the mixing-dominated zone, a negative correlation is clearly identified, supporting the evidence of a great impact of OH (or flame) on the soot oxidation process. Concerning PAH-soot (blue line), an independent spatial behavior is found in the early-formation region, due once again to spotty pattern of soot, and a

positive spatial dependence is detected in the mixing-dominated soot region. Then, considering the spatial correlation based on $P(I)$, it can be deduced that soot and PAH essentially coexist in the flame. However, since PAHs are known to be soot precursors, a strong positive relation is expected if one directly examines the signal intensities I of soot and PAHs. In Fig. 10, the instantaneous normalized soot intensity is plotted as a function of the normalized PAH intensity for both formation and mixing-dominated regions. For both zones, the highest soot intensity is found at about 20% of the maximum PAH intensity and low soot light scattering intensity values are found for high PAH intensity values. Even if precautions are necessary when using soot and PAH signal intensities to represent soot and PAH concentrations, they are certainly related to the presence of these species and could be used to examine qualitative behaviors. Here, soot mainly coexists with PAH, but soot formation and growth seem not to take place in the high PAH concentration zones. This supports the idea that soot concentration depends on flow history and local conditions and cannot be simply linked to the local volume fraction of PAHs. The previous statistical analysis could be used to validate the models derived in some recent direct numerical and large eddy simulations [6, 17, 18, 19, 20, 21].

5. Conclusions

High speed imaging provide a novel view of processes involved in the formation, interactions and destruction of soot. This reveals the spatial and temporal evolution of the layered structure of and its intermittency and allows to investigate the links between soot, OH and PAHs in turbulent flames. It is found that turbulent eddies have an important impact on the soot distribution and are responsible for the layered and highly wrinkled geometry of the regions where soot is present. An analysis of formation and mixing-dominated soot regions indicates that soot oxidation and OH presence are strongly linked. Regions where OH species is present are also regions where soot disappears. The oxidation process involving soot pockets engulfed in regions of OH at the flame tip is documented. However, more investigations are required to conclude on the role of the third spatial direction on this phenomenon. The statistical analysis proposed in this article represents a promising approach in analyzing high-speed imaging data. The imaging data obtained in the present investigation may be used to guide modeling efforts developed for the prediction of soot in large eddy and direct numerical simulations frameworks.

Acknowledgements

Thanks to Brice Villier from Hamamatsu for providing camera's intensifier and to Thomas Schmitt, Arnaud Trouvé and Nasser Darabiha for their advices in data analysis.

[1] M. Smooke, C. McEnally, L. Pfefferle, R. Hall, M. Colket, Combust. Flame 117 (1999) 117 – 139.

[2] M. Smooke, M. Long, B. Connelly, M. Colket, R. Hall, Combust. Flame 143 (2005) 613 – 628.

[3] B. Connelly, M. Long, M. Smooke, R. Hall, M. Colket, Proc. Combust. Inst. 32 (2009) 777 – 784.

[4] P. Desgroux, X. Mercier, K. A. Thomson, Proc. Combust. Inst. 34 (2013) 1713 – 1738.

[5] B. Cetegen, S. Basu, Combust. Flame 146 (2006) 687 – 697.

[6] D. O. Lignell, J. H. Chen, P. J. Smith, T. Lu, C. K. Law, Combust. Flame 151 (2007) 2–28.

[7] M. Koehler, K.-P. Geigle, T. Blacha, P. Gerlinger, W. Meier, Combust. Flame 159 (2012) 2620–2635.

[8] G. Nathan, P. Kalt, Z. Alwahabi, B. Dally, P. Medwell, Q. Chan, Prog. Energy Comb. Sci. 38 (2012) 41 – 61.

[9] S.-Y. Lee, S. R. Turns, R. J. Santoro, Combust. Flame 156 (2009) 2264 – 2275.

[10] T. L. Henriksen, G. J. Nathan, Z. T. Alwahabi, N. Qamar, T. A. Ring, E. G. Eddings, Combust. Flame 156 (2009) 1480 – 1492.

[11] V. Narayanaswamy, N. Clemens, Proc. Combust. Inst. 34 (2013) 1455 – 1463.

[12] Y. Xin, J. P. Gore, Proc. Combust. Inst. 30 (2005) 719 – 726.

[13] S. Bejaoui, X. Mercier, P. Desgroux, E. Therssen, Combust. Flame (2014) –. In press.

[14] H. Böhm, K. Kohse-Höinghaus, F. Lacas, C. Rolon, N. Darabiha, S. Candel, Combust. Flame 124 (2001) 127 – 136.

[15] C. Schulz, B. Kock, M. Hofmann, H. Michelsen, S. Will, B. Bougie, R. Suntz, G. Smallwood, Applied Physics B 83 (2006) 333–354.

[16] R. Lemaire, E. Therssen, P. Desgroux, Fuel 89 (2010) 3952 – 3959.

[17] F. Bisetti, G. Blanquart, M. E. Mueller, H. Pitsch, Combust. Flame 159 (2012) 317 – 335.

[18] H. El-Asrag, T. Lu, C. Law, S. Menon, Combust. Flame 150 (2007) 108 – 126.

[19] D. O. Lignell, J. H. Chen, P. J. Smith, Combust. Flame 155 (2008) 316 – 333.

[20] H. El-Asrag, S. Menon, Combust. Flame 156 (2009) 385 – 395.

[21] A. Attili, F. Bisetti, M. Mueller, Proc. of the Summer Program (2012) 409 – 418.

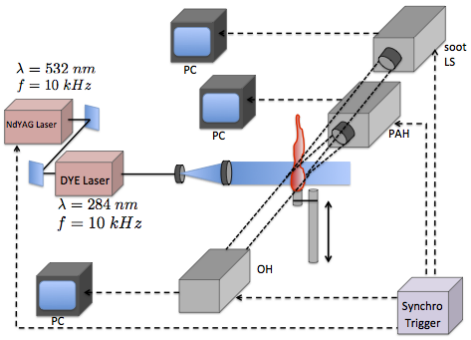

Figure 1: Schematic of the optical setup.

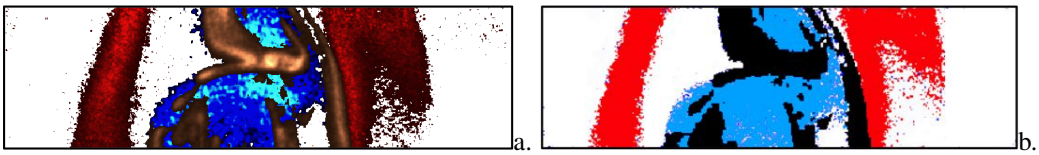

Figure 2: a) Representative snapshot of the flame structure by superimposing three simultaneous measurements. Black to red pseudo-colors represents PLIF OH signal intensity, a blue colormap is used for PLIF PAH signal and soot LS intensity is reproduced in orange. b) Presence index: OH in red, PAH in blue, soot in black.

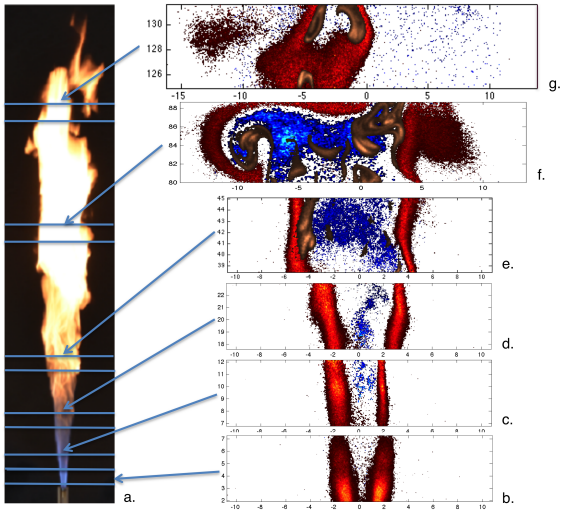

Figure 3: a) Coaxial diffusion turbulent flame. b-g) Instantaneous simultaneous PLIF PAH, PLIF OH and soot laser scattering at six measurement positions ($h = 2, 7, 17, 39, 80, 135\, d$). Scales are the same as in Fig. 2a.

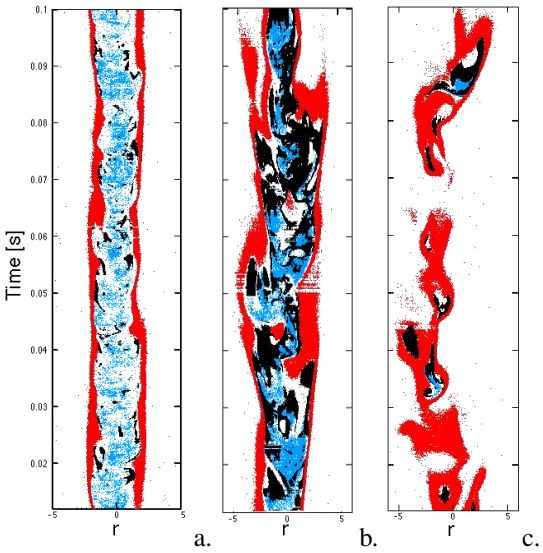

Figure 4: Temporal evolution of the presence index at the central line of the laser sheet as function of the radial position at three measurement positions: a) soot formation ($h = 35d$), b) mixing-dominated ($h = 80d$) and c)soot oxidation regions ($h = 120d$). Color caption is the same as in Fig. 2b.

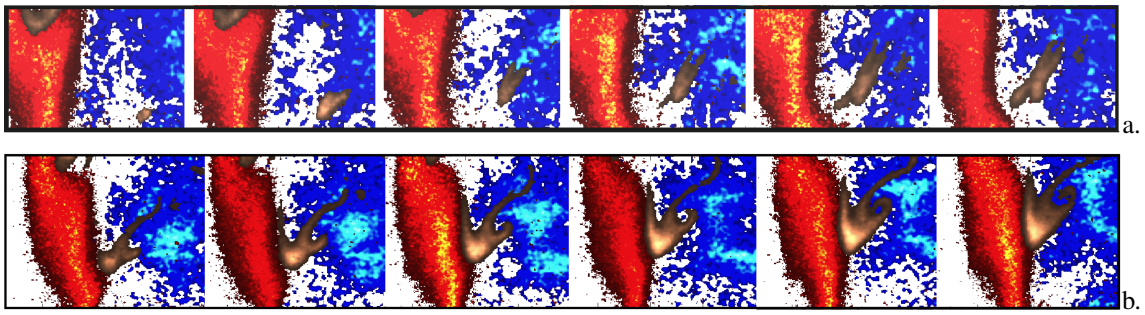

Figure 5: Temporal evolution of: a) Spotty soot growing in a ligamentary form and b) wrinkling and stretching of soot ligament due to turbulence in the early formation zone. Only one snapshot every three is visualized.

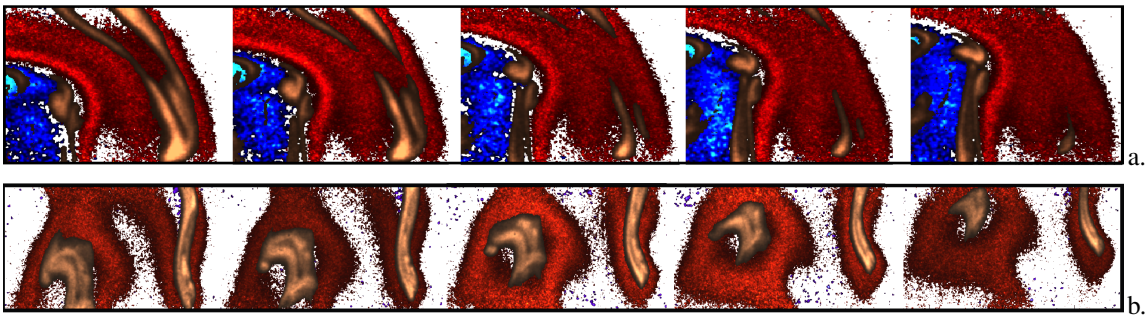

Figure 6: Temporal evolution of: a) soot-OH interaction in the mixing-dominated region and b) soot-OH pockets in the soot-oxidation zone. Only one snapshot every three is visualized.

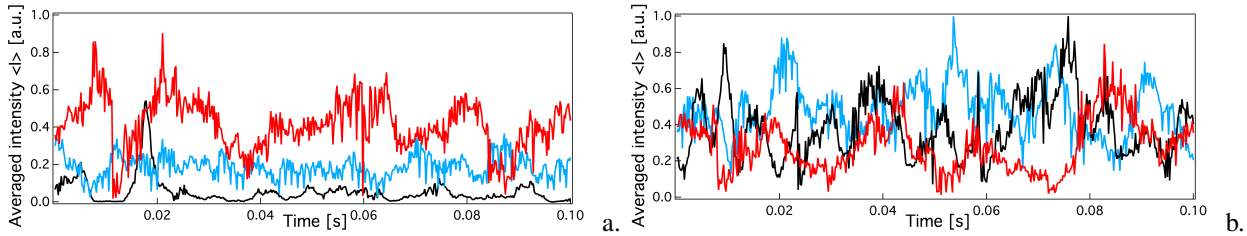

Figure 7: Temporal evolution of the normalized spatial average signal for LS (black), PLIF OH (red) and PLIF PAH (blue). Results for the a) soot formation region and b) mixing-dominated soot region.

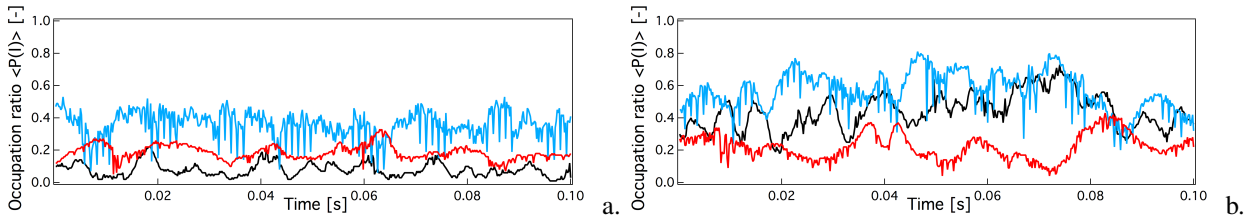

Figure 8: Temporal evolution of the occupation rate for soot (black), OH (red) and PAH (blue). Results for the a) soot formation region and b) mixing-dominated soot region.

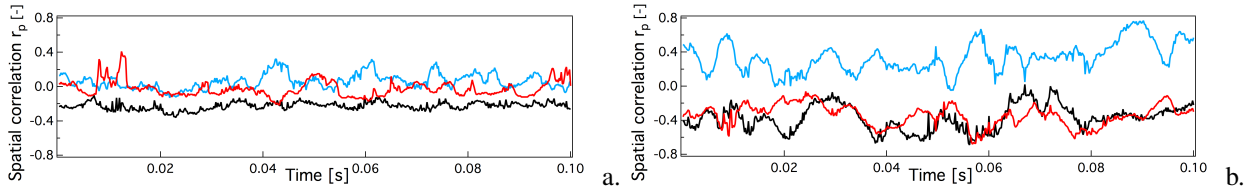

Figure 9: Temporal evolution of the correlation $r_{p_{lm}}$ between soot-OH (red), soot-PAH (blue) and OH-PAH (black). Results for the a) soot formation region and b) mixing-dominated soot region.

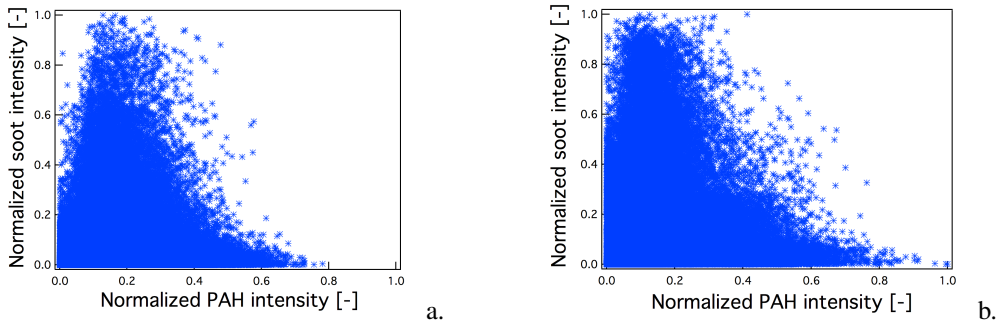

Figure 10: Normalized soot intensity signal as function of the normalized PAH intensity signal. Results for the a) soot formation region and b) mixing-dominated soot region.